Applied Catalysis B: Environment and Energy 350 (2024) 123905

Contents lists available at ScienceDirect

Applied Catalysis B: Environment and Energy

journal homepage: www.elsevier.com/locate/apcatb

Stabilization of unique $Zr^{>4+}$ species in $NiFe_2O_4$ nanocrystals for unprecedented catalytic transfer hydrogenation reaction

Mingwei Ma, Liping Li *, Xinbo Li, Qi Wang, Taotao Huang, Zhibin Geng, Ge Tian, Guangshe Li *

State Key Laboratory of Inorganic Synthesis and Preparative Chemistry, College of Chemistry, Jilin University, Changchun 130012, PR China

ARTICLE INFO

Keywords:
$Zr^{>4+}$ species
$NiFe_2O_4$ nanocrystals
Octahedral Ni sites
Electronic structure
Catalytic transfer hydrogenation reaction

ABSTRACT

Stabilization of transition metal species (like $Zr^{>4+}$) with increasingly positive charge density at oxide surfaces is highly important for intrinsically improving catalytic performance for many uses like catalytic transfer hydrogenation (CTH) reaction, which however remains inaccessible. Here, we showcase a water-quenching strategy that stably achieves $Zr^{>4+}$ species at surfaces of prototype spinel oxide $NiFe_2O_4$. Systematic investigation unveils that these $Zr^{>4+}$species were precisely incorporated into surface octahedral Ni sites of $NiFe_2O_4$. The local electronic structure was thus regulated. As a consequence, there simultaneously appear electron depletion ($Zr^{>4+}$) and accumulation (O^{2-}) at the resulted sites, which play the distinct roles as Lewis acid-base sites in (i) facilitating O-H bond dissociation and C═O bond activation, (ii) enhancing the interaction and bonding with substrate molecules, and (iii) reducing the energy barrier for hydrogen transfer process. The resulting catalysts exhibit superior catalytic performance and stability in the CTH reaction of biomass-derived carbonyls and representative aldehydes/ketones, especially the reduction of furfural to furfuryl alcohol with a yield of 90.7% under 120 ℃ for 3 h. This work provides new insights into optimizing catalytic activity in metal oxides by stabilizing transition metal species with unexpectedly positive charge density.

1. Introduction

Catalytic transfer hydrogenation (CTH) reaction is a promising alternative for the hydrogenation of renewable biomass-derived carbonyls into value-added chemicals and fuels, which uses formic acid or alcohols as H-donor instead of exogenous H_2 [1,2]. It is well documented that CTH reaction of bio-based carbonyls critically hinges the steps involving O-H bond dissociation in alcohol and C═O bond activation in substrate molecules [3,4]. Numerous investigations have indicated that Zr^{4+} ions in Zr-based catalysts play a pivotal role in this crucial step and in turn promotes catalytic performance [5,6]. Once the positive charge for Zr ions is higher than 4+ (i.e., $Zr^{>4+}$), one may find an innovative approach to significantly enhance the catalytic performance of CTH reaction [7,8], since the appearance of stable $Zr^{>4+}$ would lead to electron enrichment at O^{2-} sites in catalysts, yield stronger Lewis acid-base pairs [7,9,10], and therefore enhance C═O bond activation and O-H bond dissociation in the reaction. Metal oxides are currently employed for CTH reaction, which however encounter a bottleneck of low catalytic performance due to the relatively inert surfaces, particularly when using furfural (FAL) as a representative carbonyl [11,12]. For instance, the temperature for CTH reaction of FAL is usually in the range of 150–180 ℃ (as indicated in Table S1). As a consequence, it is highly important to find a novel strategy that could lead to metal oxides with $Zr^{>4+}$ ions incorporated, which could hopefully improve the activity and reduce the temperature of CTH reaction as well. Unfortunately, there are still no successful cases yet.

Theoretically, the synthesis of oxides that contain $Zr^{>4+}$ ions hinges on the selection of appropriate support with a tunable structure and good tolerance for doping ions. Multiple-cation based spinel oxides are a promising option due to their flexibility and structural stability [13,14]. Normal spinel structure AB_2O_4 comprises cubic packed O anions, with metal A and B cations occupying the tetrahedral (M_{Td}) and octahedral (M_{Oh}) interstices, respectively [15–17]. $NiFe_2O_4$, in contrast to other spinel oxides, exhibits a distinctive inverse spinel structure, in which Ni^{2+} overwhelmingly occupies M_{Oh} sites and Fe^{3+} distributes evenly at M_{Td} and M_{Oh} sites [18,19]. The increased configurational entropy of M_{Oh} site leads to a greater tolerance for lattice distortion, which facilitates the incorporation and stabilization of a higher concentration of

* Corresponding authors.
E-mail addresses: lipingli@jlu.edu.cn (L. Li), guangshe@jlu.edu.cn (G. Li).

https://doi.org/10.1016/j.apcatb.2024.123905
Received 30 November 2023; Received in revised form 24 February 2024; Accepted 29 February 2024
Available online 2 March 2024
0926-3373/

heterovalent metal cations at this specific site [20,21]. Meanwhile, the complex structure of $NiFe_2O_4$ promotes electrical conductivity through electron hopping between various valence states of metals within the oxygen sites, and can offer redox active metal centers for activation and adsorption of other species [12,13]. In particular, at elevated temperatures in an oxygen-rich atmosphere, such as 500 ℃, Ni^{2+} and Fe^{3+} ions in $NiFe_2O_4$ attain higher oxidation state and intense thermal ion motion [22–24]. All these factors may facilitate the ready incorporation of high-valent Zr^{4+} ions at M_{Oh} site and create the necessary conditions for generation and formation of $Zr^{>4+}$, which strictly rely on the strategy for sustained maintenance of the high valence state $Zr^{>4+}$ incorporated in the highly active $NiFe_2O_4$ at a high temperature of 500 ℃.

In this work, we initiated an innovative quenching approach to precisely introduce $Zr^{>4+}$ ions into the surface octahedral Ni sites of $NiFe_2O_4$ using water as the quenching medium. This approach is based on dual considerations: (i) liquid quenching is able to capture the high-temperature phases (like that in metallurgical process for austenite phase in high-temperature steel) [25,26], and (ii) higher oxidation states of Ni^{2+} and Fe^{3+} ions in $NiFe_2O_4$ were retained at elevated temperatures, ensuring the stable presence of $Zr^{>4+}$ ions. With such a strategy, the abundance and strength of Lewis acid-base sites in $NiFe_2O_4$-Zr nanocrystals were significantly increased. $NiFe_2O_4$-Zr nanocrystals exhibited a superior catalytic performance, achieving a reduction of furfural (FAL) within 3 h at 120 ℃, a breakthrough in the performance of CTH reaction under low temperature conditions. Density functional theory calculations, isotope tracking, and attenuated total reflectance infrared spectroscopy uncovered the mechanism of the enhanced catalytic activity. The results reported here could provide hints for tuning catalytic activity in a wide range of complex oxides with expanded functionality through creating unique high-oxidation state ions (like $Zr^{>4+}$ ions).

2. Experimental

2.1. Catalyst preparation

$NiFe_2O_4$ nanocrystals were synthesized by a coprecipitation method. In details, 40 mmol $Fe(NO_3)_3·6\ H_2O$ and 20 mmol $NiC_4H_6O_4·4\ H_2O$ were dissolved in 180 mL ethylene glycol to form a homogeneous solution under magnetic stirring. Next, the solution was heated to 150 ℃ for condensing and refluxing, and then 600 mL 0.2 M Na_2CO_3 solution was quickly added, while stirring continueously for 1 h. After cooling to room temperature, the precipitated particles were filtered, washed, and dried in vacuum at 60 ℃ to obtain the precursor. 0.5 g separated samples was calcined in air at 500 ℃ for 3 h at a heating rate of 2 ℃ min^{-1}, and then naturally cooling in muffle furnace to room temperature. The cooled sample was denoted as $NiFe_2O_4$.

For quenching experiments, 0.5 g $NiFe_2O_4$ precursor was calcined at 500 ℃ for 3 h, which was removed from the muffle furnace and immediately immersed in 20 mL high-speed stirred ice water or 0.5 M $Zr(NO_3)_4$ aqueous solution in an ice bath to achieve a rapid cooling. The samples were then obtained by filtratiing, washing and drying in vacuum at 50 ℃. The resulting samples were denoted as $NiFe_2O_4$-IQ (quenched in ice water) and $NiFe_2O_4$-Zr. Further quenching researches involved immersing $NiFe_2O_4$ in aqueous solutions that contains $Mg(NO_3)_2$, $Ce(NO_3)_3$, $Co(NO_3)_2$, $La(NO_3)_3$, $Cr(NO_3)_3$ and $Al(NO_3)_3$. The obtained samples are denoted herein as $NiFe_2O_4$-Mg, $NiFe_2O_4$-Ce, $NiFe_2O_4$-Co, $NiFe_2O_4$-La, $NiFe_2O_4$-Cr and $NiFe_2O_4$-Al, respectively. Other procedures of filtration and calcination were the same as these mentioned above.

The quenching liquid was run for 8 times to verify its recyclability. After each run, the nanocrystals were separated from the quenching liquid by a magnet, and the remaining liquid was re-used for next run. The subsequent treatment of samples was the same as the quenching procedure for preparing $NiFe_2O_4$-Zr.

2.2. Catalytic activity study

The particle sizes of the prepared catalysts $NiFe_2O_4$, $NiFe_2O_4$-IQ, and $NiFe_2O_4$-Zr are all around 5 nm. The catalytic transfer hydrogenation of bio-based carbonyls was conducted in a 15 mL ACE pressure tube that was equipped with a magnetic stirrer and immersed in a temperature-controlled oil bath. The reaction proceeded under autogenous pressure without inert gas injection. The reaction mixture, consisting of substrate (0.17 mmol), 2-propanol (5 mL), and catalyst (25 mg), was sealed in the reactor. After heating the oil bath to the specified temperature (80–160 ℃), the reactor was inserted and stirred continuously at 500 rpm for a designed time (0.5–8 h). When the set time was over, the reaction vessel was removed from the oil bath and cooled naturally. Then, the liquid product was qualitatively analysed by TRACE ISQ GC-MS (TR–WAX–MS column 30.0 m × 320 μm × 0.25 μm). The conversion of furfural (FAL), yield and selectivity of furfuryl alcohol (FOL) were defined as follows:

$$\text{FAL conversion}(\%) = \left(1 - \frac{Mole\ \ of\ \ FAL}{Initial\ \ mole\ \ of\ \ FAL}\right) \times 100\% \tag{1}$$

$$\text{FOL yield}(\%) = \frac{Mole\ \ of\ \ FOL}{Initial\ \ mole\ \ of\ \ FAL} \times 100\% \tag{2}$$

$$\text{FOL selectivity}(\%) = \frac{Mole\ \ of\ \ FOL}{Initial\ \ mole\ \ of\ \ FAL - Mole\ \ of\ \ FAL} \times 100\% \tag{3}$$

To assess the reusability of the as-prepared $NiFe_2O_4$-Zr nanocrystals, 8 consecutive reaction runs were conducted at 120 ℃ with a reaction time of 1 h. After each run, the catalyst, separated from the reaction system by a magnet, underwent a washing step with 5 mL of ethanol. Subsequently, it was dried in vacuum at 60 ℃ for 1 h before being employed in the subsequent run. The product analysis procedure followed that previously described.

A scaled-up experimental investigation of CTH reaction was carried out using a 300 mL stainless steel autoclave (JULABO). In this scaled-up setup, the autoclave was loaded with FAL (10 mmol), 2-PrOH (150 mL), and a catalyst (1 g). Subsequently, the autoclave was sealed and subjected to heating at 120 ℃ for a duration ranging from 1 to 6 h.

2.3. Characterizations

All characterizations are available in the Supporting Information.

2.4. DFT calculations

All the density functional theory (DFT) calculations can be found in Supporting Information.

3. Results and discussion

3.1. Preparation of $NiFe_2O_4$-Zr nanocrystals

$NiFe_2O_4$-Zr nanocrystals with $Zr^{>4+}$ ions were first prepared by a water quenching method (namely, heated $NiFe_2O_4$ was rapidly cooled in a Zr^{4+} solutions at 0 ℃, as shown in Fig. 1a, please see details in *2.1 Catalyst preparation* section). During the quenching process, $NiFe_2O_4$ underwent a lattice expansion with elevated valence state of metal cations, and an intense thermal ion motion was induced in air at 500 ℃ [22,23]. Subsequently, the heated $NiFe_2O_4$ was rapidly immersed in Zr^{4+} solution at 0 ℃, enabling Zr^{4+} to enter the activated and high-valent surface of $NiFe_2O_4$. A rise in configurational entropy within M_{Oh} sites containing Fe^{3+} and Ni^{2+} results in a greater tolerance for doping heterovalent metal cations [20,21]. Thus, Zr^{4+} exhibits a preference for incorporation into the surface M_{Oh} sites. The ionic radius difference between Zr^{4+} (0.72 Å) and Ni^{2+} (0.69 Å) is 0.03 Å, while that between Zr^{4+} (0.72 Å) and Fe^{3+} (0.65 Å) is 0.07 Å. Zr^{4+} ions could

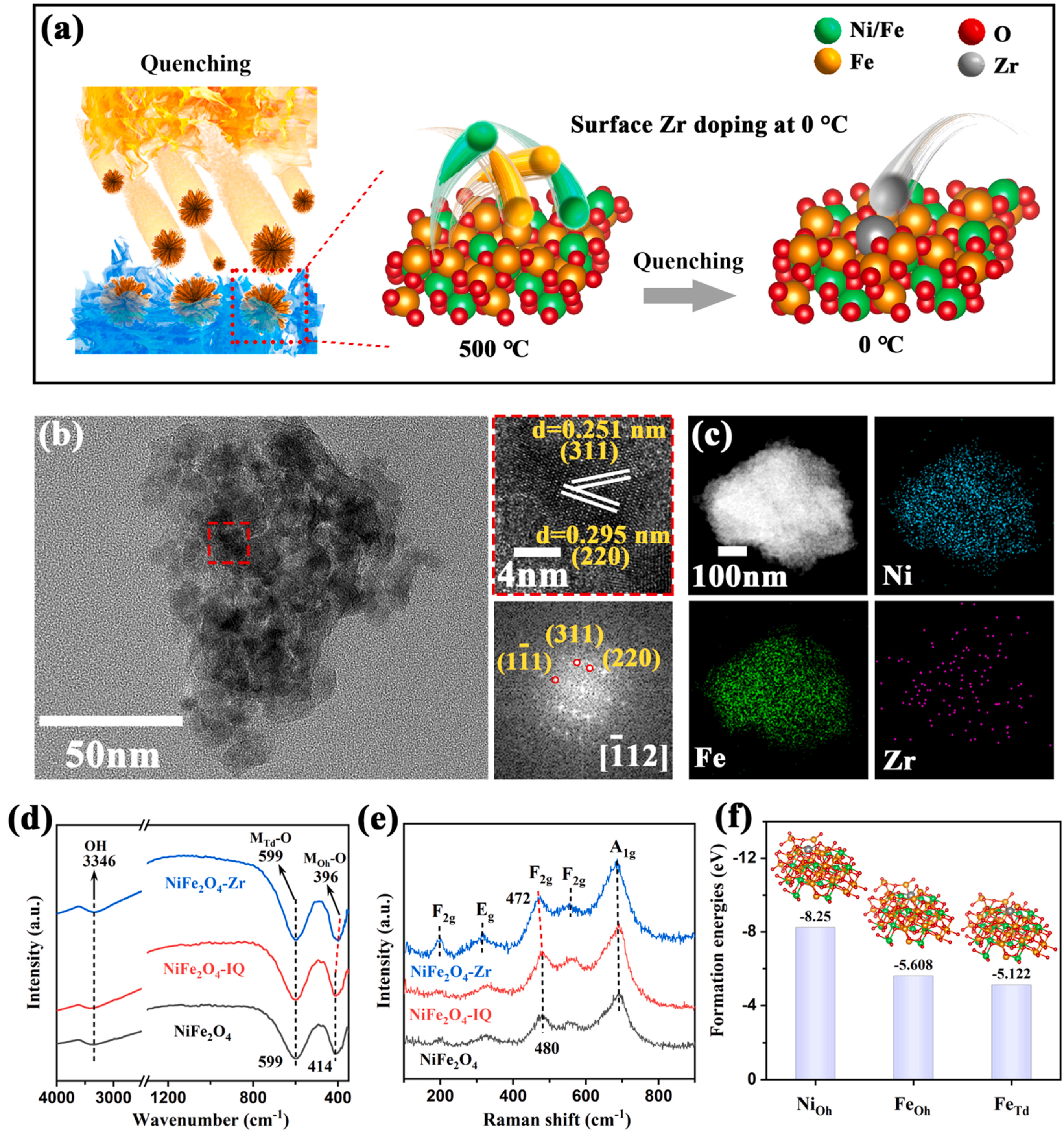

Fig. 1. Preparation and structural characterization of the $NiFe_2O_4$ nanocrystals. (a) Schematic illustration of the quenching method used to prepare $NiFe_2O_4$-Zr nanocrystals; (b) TEM and HRTEM images, (c) HAADF-STEM and corresponding elemental mapping images; (d) FT-IR spectra; and (e) Raman spectra of the samples; (f) Formation energies calculated for Zr doping at Ni_{Oh}, Fe_{Oh} and Fe_{Td} sites of $NiFe_2O_4$.

preferentially occupy the surface octahedral Ni sites. The higher oxidation states of the spinel oxide surface at high temperatures will promote the production of $Zr^{>4+}$ with a higher positive charge. As a result, $Zr^{>4+}$ species was successfully incorporated in $NiFe_2O_4$ nanocrystals through a water quenching process.

Sample morphologies before and after water-quenching treatment were monitored by scanning electron microscopy (SEM) and transmission electron microscopy (TEM). All samples $NiFe_2O_4$ showed a similar structure stacked by grains with sizes around 6 nm (Figs. 1b, S1, S2). The lattice spacings were observed to be 0.295 nm and 0.251 nm in the high-resolution TEM (HRTEM) image, which can be assigned to the (220) and (311) crystalline planes of $NiFe_2O_4$ (Figs. 1b, S2). A crystal axis [$\bar{1}$12] was evidenced for the particle in selected area electron diffraction by Fast Fourier transformation (FFT). The crystal structure of untreated $NiFe_2O_4$ and quenched $NiFe_2O_4$-IQ remained the same as $NiFe_2O_4$-Zr nanocrystals, and the components Fe, Ni, and Zr were uniformly distributed in the products from high-angle annular dark-field scanning transmission electron microscopy (HAADF-STEM) and the

corresponding EDS mapping images (Fig. 1c). Furthermore, Fe/Ni molar ratio for all $NiFe_2O_4$ nanocrystals are closer to 2:1. Table S2 And the Fe/Ni/Zr molar ratio of $NiFe_2O_4$-Zr nanocrystals is 2.14:1:0.02.

Crystal structures of the samples were examined in details using X-ray diffraction (XRD) patterns, Fourier transform infrared (FT-IR) spectra, and Raman spectra. All samples, regardless of directly calcined or undergoing a quenching process, showed a well-crystallized cubic spinel $NiFe_2O_4$ phase with space group of *Fd-3 m* (Figure S3a), well matching the standard data (JCPDS, No. 10–0325). These observations are in line with the analysis of HRTEM (Fig. 1b). The primary particle size was determined to be about 5 nm using Scherrer equation (Table S2). No other impurity phases were detected, indicating a high phase purity. FT-IR spectra and Raman spectra are used to further study the lattice features of samples, including composition, bonding, and chemical environment. Samples exhibits the similar FT-IR spectra (Fig. 1d), in which two absorptions at ~599 and ~400 cm^{-1} are attributed to the stretching vibration modes of tetrahedrally coordinated M_{Td}-O bonds and octahedrally coordinated M_{Oh}-O bonds in spinel structure, respectively [12,27]. It is noted that M_{Oh}-O bond of $NiFe_2O_4$-Zr nanocrystals showed a red-shift to 396 cm^{-1} comparing to those of other two samples (414 cm^{-1}), while the absorption representing M_{Td}-O bond did not show any shift. According to the formula for molecular vibration wave number (see details in *1.5 Molecular vibrational wavenumber* section of the Supporting Information), it could be seen that a red shift in wavenumber could result from a decrease in the vibration potential energy constant (k) and an increase in the reduced mass (μ). Such a reduction in k is attributed to an increase in bond length. Consequently, when Zr, with a higher molar mass, occupies the octahedral sites, k decreases and μ increases, leading to a red shift of the absorption position for octahedral sites. This observation could be explained in terms of the alteration in molecular bonding of Ni/Fe–O within $NiFe_2O_4$ when Zr replaces Ni or Fe at octahedral sites.

Raman spectra of the samples exhibited five similar vibration peaks as marked in Fig. 1e, which agree with the Raman active modes of cubic

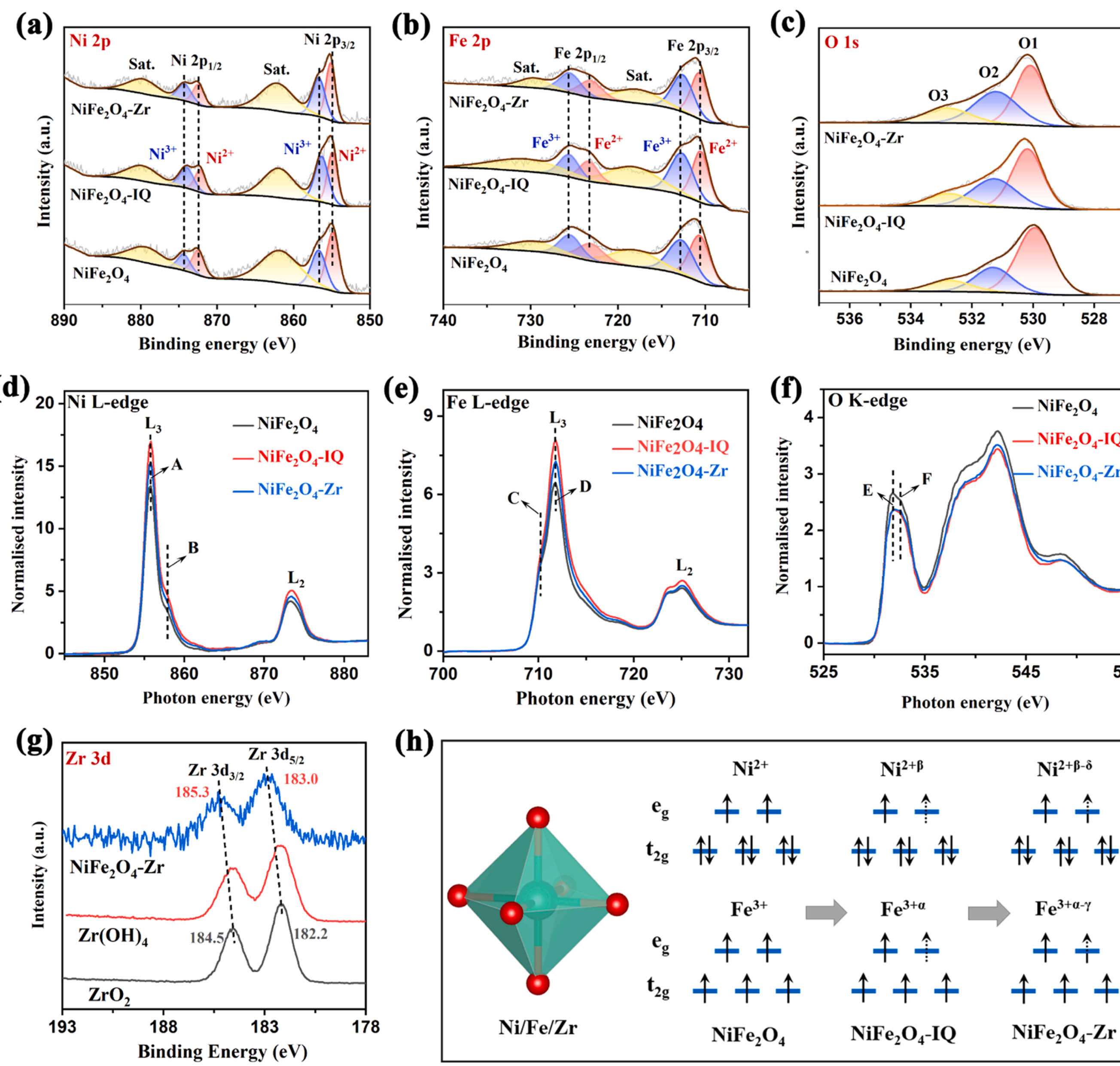

Fig. 2. Surface composition and electronic states of the $NiFe_2O_4$ nanocrystals. XPS spectra of (a) Ni 2p, (b) Fe 2p, (c) O 1 s, and (g) Zr 3d; XAS spectra for (d) Ni L-edge, (e) Fe L-edge, and (f) O K-edge XANES; (h) Schematic electronic configuration of the cations at octahedral sites.

spinel structure. The lower wavenumbers of F_{2g} (480 cm^{-1}) mode correspond to the octahedral sites, while A_{1g} (687 cm^{-1}) mode is attributed to the tetrahedral sites [12,28,29]. When the vibrational peak of the octahedral unit was selectively amplified (Figure S3b), a distinct red-shift in $NiFe_2O_4$-Zr is observed, providing further evidence for Zr doping at the octahedral site. From the crystal structures of $NiFe_2O_4$-Zr optimized by Density functional theory (DFT) as listed in Figure S4, one can see that the calculated formation energy of one Zr atom doped at surface Ni_{Oh} (−8.25 eV) site is lower than those for other dopings at surface Fe_{Oh} (−5.608 eV) and Fe_{Td} (−5.122 eV) sites of $NiFe_2O_4$ (Fig. 1f). That is, Zr^{4+} ions prefer to occupy surface Ni_{Oh} sites.

3.2. Understanding the changes in surface composition and electronic structure of $NiFe_2O_4$-Zr nanocrystals

Surface composition of $NiFe_2O_4$-Zr nanocrystals was analyzed by X-ray photoelectron spectroscopy (XPS). From Table S2, one can see that Zr^{4+} species prefers to occupy the surface sites of $NiFe_2O_4$ nanocrystals, because Zr wt% measured by XPS is much larger than that by ICP. Moreover, Zr^{4+} predominantly located at the surface Ni_{Oh} sites, as indicated by the combined analyses of DFT calculation, FT-IR spectra, and Raman spectra.

M_{Oh} is preferentially exposed on the surface of spinel oxides, while M_{Td} is almost undetectable at surface [17,30]. This dominance is due to the significant overlap between e_g orbital of M_{Oh} and 2p orbital of oxygen (O), resulting in robust σ interactions that facilitate catalytic reactions, as reported in other systems [13,14,17]. Hence, by controlling the electron occupation of e_g orbital at Ni_{Oh} and Fe_{Oh} sites, the regulation of the surface electronic structure of $NiFe_2O_4$-Zr nanocrystals could enable the formation and stability of $Zr^{>4+}$. Insight into the quenching-induced changes in electronic structural state of $NiFe_2O_4$ nanocrystals was gained using XPS spectra (Fig. 2). The fine-scanned Ni 2p spectra revealed six distinct signals (Fig. 2a) that correspond to Ni^{2+} (854.9 and 872.4 eV), Ni^{3+} (856.3 and 874.3 eV), and satellite peaks (862.1 and 879.8 eV), following the assignments in literature [18]. The ratios of Ni^{3+} to Ni^{2+} in $NiFe_2O_4$-Zr and $NiFe_2O_4$-IQ are determined to be 0.92 and 1.17, which are both higher than that of 0.72 in $NiFe_2O_4$ (Table S3). Based on these ratios, the average e_g filling rate of Ni cations in $NiFe_2O_4$-Zr was calculated to be 1.52, slightly lower than that of 1.58 in $NiFe_2O_4$, but higher than that of 1.46 in $NiFe_2O_4$-IQ. Fe 2p XPS spectra recorded from 705 to 740 eV show a change in electronic structure resembling that in Ni 2p XPS spectra (Fig. 2b, Table S3). Based on Ni 2p and Fe 2p XPS data analyses, the quenching process preserves the high oxidation state of Ni and Fe in the heated $NiFe_2O_4$, signifying that heated $NiFe_2O_4$ functions as an open and highly active acceptor, conducive to the formation and stability of $Zr^{>4+}$. Therefore, introduction of Zr^{4+} to the activated and high-valent surface of $NiFe_2O_4$ during quenching process would inevitably lead to a rearrangement of the surface composition and electronic structure, providing a crucial foundation for the formation and stability of $Zr^{>4+}$ doped at the surface Ni_{Oh} sites and moderate e_g filling. O 1 s spectra of all samples were deconvoluted into three peaks at 530.1, 531.2, and 532.8 eV (Fig. 2c), corresponding to lattice oxygen (O1), hydroxyl oxygen (O2), and adsorbed water (O3), respectively [31]. The O2/(O1+O2+O3) ratio follows the trend, $NiFe_2O_4$-Zr (36%) > $NiFe_2O_4$-IQ (34%) > $NiFe_2O_4$ (24%) (Table S3). Obviously, the quenching method employed in this work could induce the generation of surface hydroxyl, thereby can provide a strong base sites for CTH reaction [10]. In Zr 3d XPS spectra (Fig. 2g), signals at 185.3 and 183.0 eV are attributed to Zr $3d_{3/2}$ and Zr $3d_{5/2}$, respectively. Notably, the binding energy of Zr for $NiFe_2O_4$-Zr is higher than those for ZrO_2 and $Zr(OH)_4$. This observation may be due to the electron transfer from Zr ions to Ni, Fe, and O ions within $NiFe_2O_4$-Zr, resulting in the emergence of $Zr^{>4+}$. Such a charge transfer between Zr and other ions was more intuitively indicated by a subsequent differential charge distribution of $NiFe_2O_4$-Zr via DFT (Fig. 4c). In short, the quenching process activates $NiFe_2O_4$, leading to a high oxidation state surface that enables the formation of $Zr^{>4+}$, which could regulate the surface composition and local electronic structure of $NiFe_2O_4$.

Electronic structures were further characterized by X-ray absorption spectroscopy (XAS). From Ni L-edge and Fe L-edge spectra, one can see that peaks A and B correspond to Ni 3d t_{2g} and e_g orbitals, respectively, while peaks C and D can be attributed to Fe 3d t_{2g} and e_g orbitals (Figs. 2d, 2e) [19,32]. The ratios of peaks B to A and peaks D to C were listed in Table S4. It is noted that these ratios increase following the quenching process due to the high valence states of Ni and Fe cations in $NiFe_2O_4$-IQ providing empty e_g orbitals that promote the transition probability, as reported elsewhere. This suggests that the quenching process activates $NiFe_2O_4$ in favor of doping modifications, consistent with XPS data analysis. Therefore, this ratio appears to decrease due to the fact that high oxidation states Ni and Fe prompt the formation and stability of $Zr^{>4+}$ to cause electronic structure rearrangement, thereby obtaining moderate e_g filling.

O K edge is also instrumental in elucidating the electronic structure of materials. Typically, peaks in the lower energy range, denoted as peaks E and F, reflect the splitting of O 2p hybridized orbitals with metal 3d t_{2g} and e_g orbitals (Fig. 2f) [33,34]. The intensity ratio of peak F to E noticeably increased after quenching relative to $NiFe_2O_4$, indicating an increased transition probability of electrons from O 1 s to e_g orbitals (Table S4). These findings corroborate the earlier XPS results, demonstrating that the quenching process effectively modulates the electron occupancy from high electron occupation $Ni^{2+}(t_{2g}^6e_g^2)/Fe^{3+}(t_{2g}^3e_g^2)$ in $NiFe_2O_4$ to low electron occupation $Ni^{2+\beta}(t_{2g}^6e_g^{2+\beta})/Fe^{3+\alpha}(t_{2g}^3e_g^{2+\alpha})$, as reported elsewhere [13,35]. Such a change in electric occupation is conducive to the rearrangement of the structure caused by subsequent doping. Therefore, introduction of Zr^{4+} during quenching regulates the electron occupancy at an intermediate level $Ni^{2+\beta-\delta}(t_{2g}^6eg^{2+\beta-\delta})/Fe^{3+\alpha-\gamma}(t_{2g}^3e_g^{2+\alpha-\gamma})$ due to the electron supplementation provided by Zr^{4+} (Fig. 2h), which indicates the formation of $Zr^{>4+}$. The above results demonstrate that the selective doping of $Zr^{>4+}$ to the surface Ni_{Oh} sites of $NiFe_2O_4$ is successfully achieved via quenching in Zr^{4+} solution, in which the sample surface is reconfigured, and correspondingly its electronic structure is well modulated.

3.3. Quantitative analysis of acid-base active sites

Regulation of surface composition and electronic structure has a significant impact on the activity of acid-base sites, which plays a crucial role in determining CTH reaction [5,10,36,37]. In comparison to untreated $NiFe_2O_4$, the particle size, specific surface area, and pore size of $NiFe_2O_4$-IQ and $NiFe_2O_4$-Zr nanocrystals after quenching remained largely unchanged (Tables S2 and S5, Figures S5a and S5b), avoiding variations in size effects that could impact the catalytic active sites and their performance. The acid-base properties could be gained preliminary insight through the analysis of the above-mentioned electronic structures. Decreased intensity in O K-edge spectrum, accompanying with the increased intensity of Ni L-edge and Fe L-edge peak for quenched $NiFe_2O_4$-IQ and $NiFe_2O_4$-Zr (Figs. 2d-2f), suggests a higher electron density at O site and a lower electron density at Ni/Fe site, and an increased polarity of the metal-oxygen bond [38,39]. Similarly, $Zr^{>4+}$ also has a low electron density (Fig. 2g). In general, for cations like Ni, Fe and Zr, the lower the electron density and the emptier the 3d/4d orbitals, the more or stronger Lewis acids are produced. Regarding O, higher electron density around O species could provide more or stronger Lewis bases. Consequently, both the samples, quenched $NiFe_2O_4$-IQ and $NiFe_2O_4$-Zr show Lewis acid-base sites.

To gain a deeper insight into the impact of quenching on the acid-base properties of the samples, temperature-programmed desorption ($NH_3/CO_2/O_2$-TPD) experiments were evaluated using probe molecules NH_3, CO_2, and O_2. Comparing to $NiFe_2O_4$ and $NiFe_2O_4$-IQ, the sample $NiFe_2O_4$-Zr exhibits more and higher desorption peaks due to the change of surface electronic structure induced by Zr introduction, which further proves that $NiFe_2O_4$-Zr has more and stronger acid-base sites

(Figures S5c, S5d). A new desorption peak at ~250 ℃ in NH_3/CO_2-TPD profiles of quenched $NiFe_2O_4$-Zr is related to the active O species and Zr cations introduced during the quenching process. This is confirmed by O_2-TPD profiles (Figure S5e), in which the peak appeared between 200 and 400 ℃ is attributed to the desorption peak of surface lattice oxygen [40], and a higher desorption amount for $NiFe_2O_4$-Zr indicates the presence of more active oxygen species. The data relevant to the acid-base concentration of samples are summarized in Figure S5f, in which $NiFe_2O_4$-Zr has demonstrated to show a highest acid-base concentration among all samples.

3.4. Reaction evaluations toward CTH reaction

The promotion of $NiFe_2O_4$ nanocrystals for CTH reaction by the introduction of $Zr^{>4+}$ during quenching was investigated by selecting the hydrogenation of FAL as the probe reaction with 2-PrOH as both solvent and H-donor. During the initial catalytic test, we evaluated the catalytic performance of all samples at 120 ℃ for a duration of 1 h, and the obtained results are presented in Fig. 3a. Compared with inactive $NiFe_2O_4$, all quenched $NiFe_2O_4$ nanocrystals exhibited significant catalytic activities. Specifically, $NiFe_2O_4$-IQ has a FOL yield of 57.6% after ice-bath quenching better than $NiFe_2O_4$ (FOL yield of 45.5%), but inferior to quenched $NiFe_2O_4$-Zr (FOL yield of 71.9%), and even worse than other samples synthesized by quenching metal doping (Mg, Ce, Co, La, Cr and Al). It may be attributed to the surface composition and local electronic structure regulated by the surface-doped metal. The catalytic performance of $NiFe_2O_4$-Zr nanocrystals was investigated in terms of reaction temperature and time (Fig. 3c). Conversion and yield were improved with increasing the values of both parameters. To further elucidate the relationship between various $NiFe_2O_4$ nanocrystals and their catalytic activity at varying reaction temperatures and times, kinetic experiments for CTH reaction of FAL to FOL were conducted in 2-PrOH (Fig. 3b and Figure S6). Figures S6a–S6c showed a linear correlation between $\ln(C_t/C_0)$ and reaction time at each reaction temperature, indicating first-order kinetics of CTH reaction for $NiFe_2O_4$ nanocrystals from FAL to FOL. With the Arrhenius equation ($\ln k = E_a/RT + \ln A$), the apparent activation energy (E_a) for the CTH reaction of FAL was determined (Figures S6d-S6f). $NiFe_2O_4$-Zr exhibited an Ea of 44.37 kJ mol^{-1}, smaller than those for $NiFe_2O_4$-IQ (52.95 kJ mol^{-1}) and $NiFe_2O_4$ (56.61 kJ mol^{-1}), which indicates that CTH reaction proceeds more easily with $NiFe_2O_4$-Zr, attributable to the regulation of composition and electronic structure achieved by $Zr^{>4+}$ doping.

The magnetic properties of $NiFe_2O_4$ nanocrystals were analyzed using a superconducting quantum interference device-vibrating sample magnetometer (SQUID-VSM) (Figure S7). Magnetization hysteresis curve displayed a small remanence and coercive force, indicating a strong superparamagnetic behavior, as reported elsewhere [41]. All three samples exhibited magnetic saturation values of approximately 20 emu/g. Notably, as depicted in inset of Fig. 3e, $NiFe_2O_4$-Zr nanocrystals in the reaction mixture were rapidly separated using an external magnet, eliminating the need for complex filtration or centrifugation. All these features allow the practical application as magnetic catalysts. Subsequently, the reusability and heterogeneity of the magnetic $NiFe_2O_4$-Zr nanocrystals were evaluated by leaching and recycling experiments. $NiFe_2O_4$-Zr nanocrystals show an excellent reusability, maintaining their catalytic performance over at least 8 cycles (Fig. 3e).

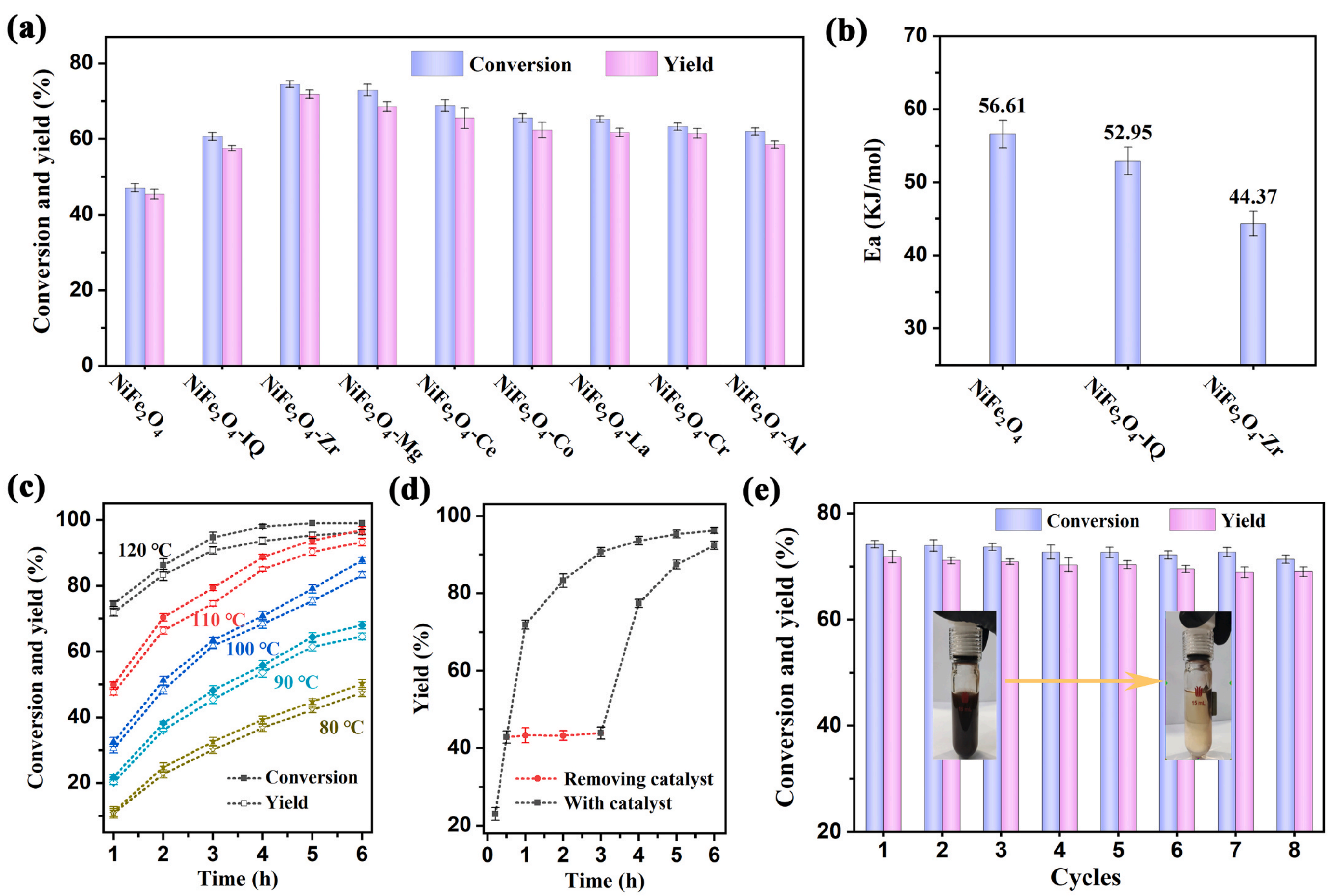

Fig. 3. CTH activities of $NiFe_2O_4$ nanocrystals. (a) CTH reaction of FAL over various catalysts at 120 ℃ for 1 h; (b) E_a of different $NiFe_2O_4$ for CTH reaction of FAL; (c) Change of the performance of $NiFe_2O_4$-Zr with reaction temperature and time; (d) Leaching experiment and (e) reusability of $NiFe_2O_4$-Zr for CTH reaction of FAL. Conditions: FAL (0.17 mmol), catalysts (25 mg), 2-PrOH (5 mL), 120 ℃ and 1 h.

After each cycle, the catalyst was effortlessly recovered using an external magnet, washed with de-ethanol thrice, and dried in vacuum at 60 ℃ for 1 h before the next cycle. Furthermore, the used catalysts retained a stable physicochemical property, as depicted in Figure S8 and Table S6, highlighting an excellent stability during the CTH reaction. To further prove the heterogeneous nature of $NiFe_2O_4$-Zr nanocrystals, two parallel experiments were conducted: one with the catalyst separated from the reaction mixture after 1 h and re-added after 3 h, and another without separation (Fig. 3d). No reaction was observed in the system without catalyst, and Zr, Ni, and Fe Species were not detected in the filtrate within the detection limit of ICP, suggesting that the metal ions in the catalyst were not leached. This result confirms the heterogeneous and

Table 1
CTH reaction of different carbonyl compounds over $NiFe_2O_4$-Zr nanocrystals.

Entry	Reactant	Main product	Temp. (℃)	Time (h)	Conv. (%)	Yield (%)
1	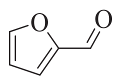	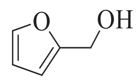	120	3	94.6±1.7	90.7±1.1
2	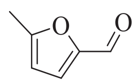	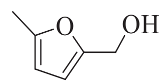	130	6	87.4±1.3	85.1±0.9
3	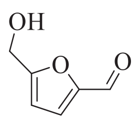	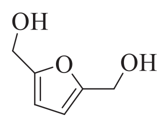	130	8	90.1±1.8	86.3±1.4
4	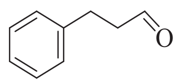	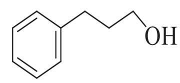	120	6	92.4±1.2	90.0±1.7
5	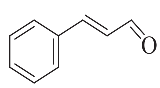	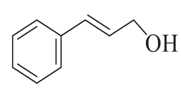	130	5	90.5±1.6	86.4±1.4
6	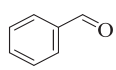	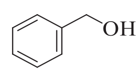	120	4	95.0±1.3	93.2±1.4
7	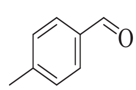	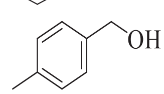	120	8	86.0±3.3	84.2±2.7
8	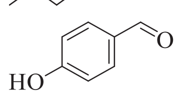	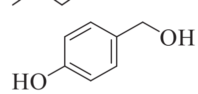	120	8	76.1±1.9	73.1±2.1
9	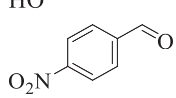	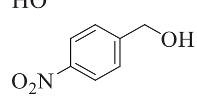	120	6	90.0±1.9	87.6±2.2
10	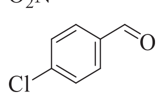	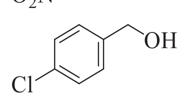	120	6	91.6±1.5	89.6±1.0
11	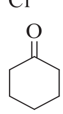	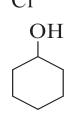	160	5	95.0±1.9	92.1±1.7
12	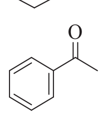	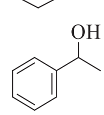	160	5	92.6±1.6	90.6±1.7
13	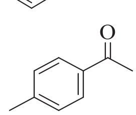	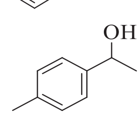	160	5	84.7±1.7	82.9±1.2
14	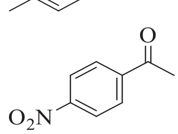	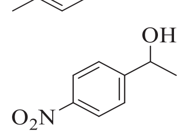	160	5	89.6±1.4	88.1±1.3
15	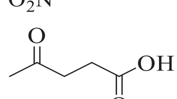	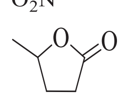	160	5	92.7±1.9	87.2±2.2
16	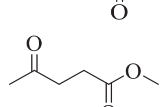	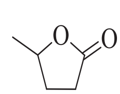	160	5	86.6±1.9	82.4±1.4

Conditions: catalyst (25 mg), substrate (0.17 mmol), and 2-propanol (5 mL).

stability of $NiFe_2O_4$-Zr.

Encouraged by the outstanding performance of $NiFe_2O_4$-Zr nanocrystals in the CTH reaction of FAL to FOL, several application potential tests were explored, included recyclability of quenching liquid, selecting appropriate alcohol sources, assessing the broader applicability of carbonyls hydrogenation and conducting scaled-up CTH reaction (detailed discussion in the Supporting Information, Figure S9). While the reusability of the quenching liquid is maintained, the $NiFe_2O_4$-Zr nanocrystals maintains high catalytic activity, highlighting the potential of the quenching liquid for ultra-long reusability (Figures S9a-S9c). The chemical nature of the alcohol sources as H-donor directly influences the catalytic activity of CTH reaction. Secondary alcohols perform better as H-donor due to stronger hydrogen supply than primary alcohols, while tert-butanol shows almost no activity (Figure S9e). Furthermore, the suitability of $NiFe_2O_4$-Zr nanocrystals was assessed using a wide range of substrates, including biomass-derived carbonyls and representative aldehydes and ketones (Table 1). The catalyst demonstrates an efficient conversion of these substrates into the corresponding alcohols through CTH reaction. To evaluate the potential of the catalyst for large-scale production of FOL from FAL, a CTH scale-up experiment was performed using 10 mmol of FAL as the substrate, which maintained a high catalytic performance during the scale-up process (Figures S9d and S9f). These verification results highlight the application prospects of $NiFe_2O_4$-Zr nanocrystals.

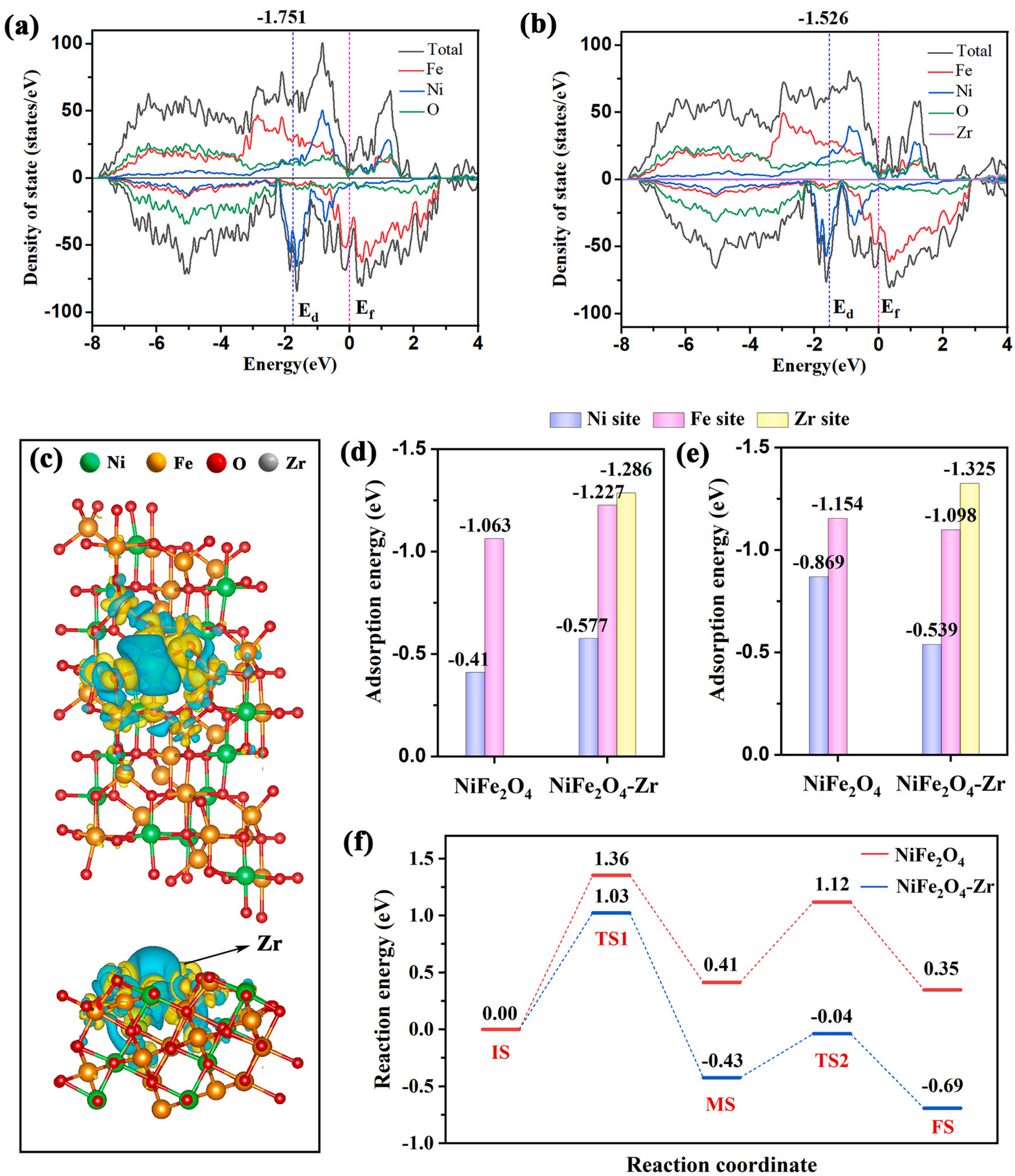

Fig. 4. Density functional theory calculations of relevant theoretical models. Density of states (DOS) of (a) $NiFe_2O_4$ and (b) $NiFe_2O_4$-Zr; (c) Differential charge density distributions of $NiFe_2O_4$-Zr, with the cyan and yellow colors representing electron depletion and accumulation regions, respectively; Calculated adsorption energies of (d) FAL and (e) 2-PrOH molecules by respectively selecting Ni, Fe and Zr as the adsorption sites in $NiFe_2O_4$ and $NiFe_2O_4$-Zr; (f) Calculated hydrogenation free energy profiles of FAL on the surface of $NiFe_2O_4$ and $NiFe_2O_4$-Zr. (For interpretation of the references to color in this figure legend, the reader is referred to the web version of this article.)

3.5. Identifying the mechanism

To reveal the atomic origin behind the improved CTH activity of $NiFe_2O_4$-Zr, DFT calculations were carried out to compare the electronic properties of $NiFe_2O_4$ with or without Zr. The change in electronic structure can also be observed from the d-band of $NiFe_2O_4$ and $NiFe_2O_4$-Zr, with the d-band center (E_d) value relating to the binding strength of the intermediate to the active site and the catalytic activity [12,14]. In comparison to $NiFe_2O_4$ (-1.751 eV), the E_d value of $NiFe_2O_4$-Zr (-1.526 eV) exhibits a closer proximity to the Fermi level (E_f) (Figs. 4a and 4b), signifying a positive shift of the d-band center. This highlights the significant role played by the occupation of Ni_{Oh} sites on the surface of $NiFe_2O_4$ by Zr in the regulation of electronic structure. For $NiFe_2O_4$-Zr, substitution of Zr cations for surface octahedral Ni sites enables a greater electron accumulation in anti-bonding states at the Fermi level. This upward shift of d-band center results in the augmentation of chemisorption stability between the substrate molecules and the active centers. The charge density difference diagram confirms that the existence of Zr^{4+} induces a charge redistribution (Fig. 4c). Zr^{4+} undergoes a significant electron transfer to nearby Ni, Fe, and O, decreasing the electron density of Zr while increasing the electron density of Ni, Fe, and O, thereby promoting the formation of $Zr^{>4+}$, in agreement with XAS and XPS analyses. Therefore, Zr doping plays a crucial role in efficiently modulating the electronic structure of $NiFe_2O_4$, thereby promoting the CTH reaction of FAL.

The CTH reaction of FAL necessitates three pivotal stages: (1) dehydrogenation of hydrogen donors, (2) hydrogenation of hydrogen acceptors, and (3) transfer of active hydrogen from 2-PrOH to FAL substrates. This process occurring at the catalyst surface entails O-H bond dissociation and C=O bond activation to facilitate a hydrogen

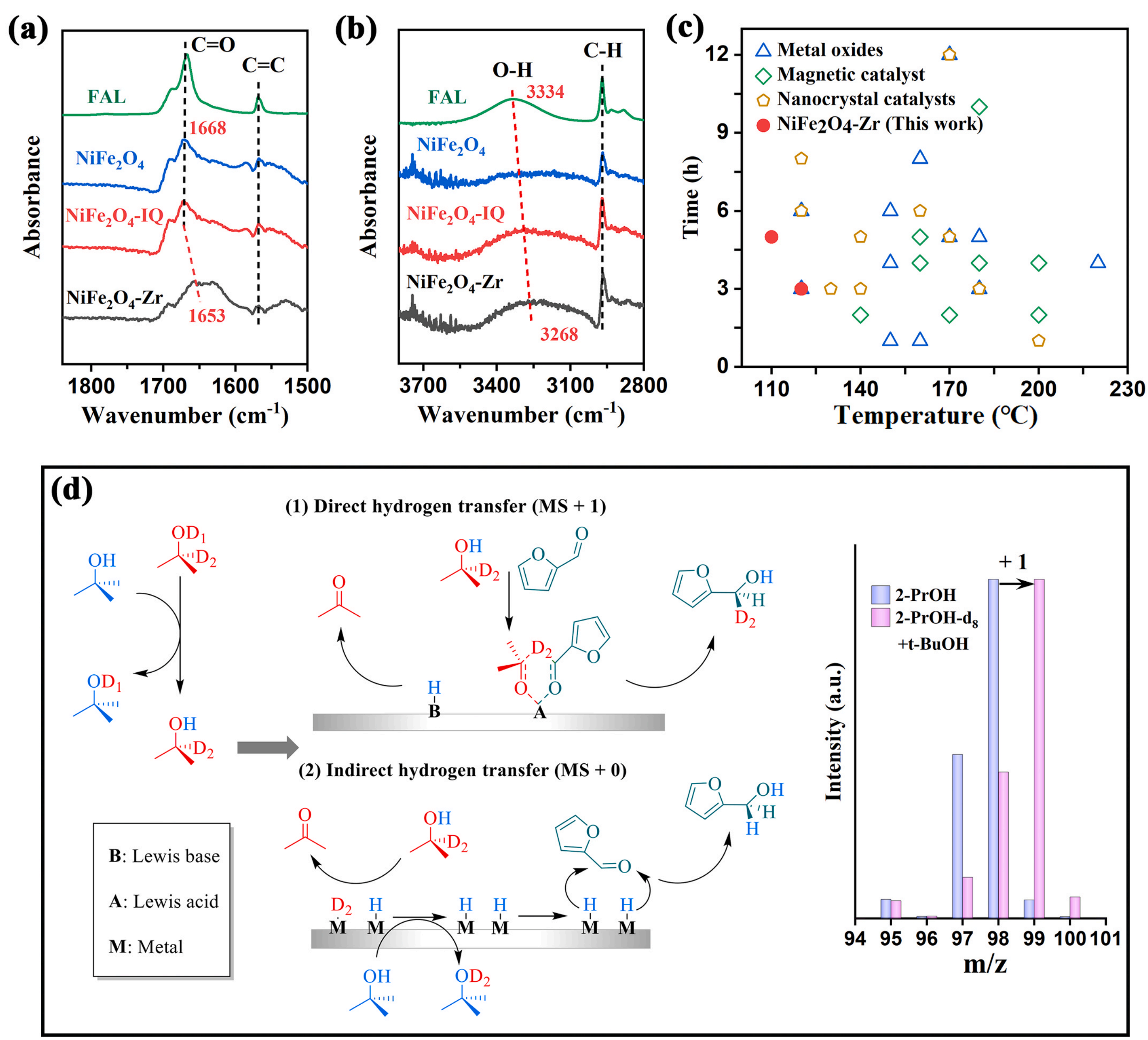

Fig. 5. Mechanism investigations. ATR-IR spectra of the adsorption of (a) FAL and (b) 2-PrOH over different catalysts; (c) Comparison of the optimal catalytic performance profiles of sample $NiFe_2O_4$-Zr with various metal oxides, magnetic catalysts and nanocrystal catalysts for the CTH reaction of FAL in temperature and time dimensions; (d) Schematic of the reaction mechanism via direct hydrogen transfer or indirect hydrogen transfer, and the mass spectra of FOL obtained from FAL hydrogenolysis in different solvents (2-propanol and 2-PrOH-d8+t-butanol). Conditions: FAL (0.17 mmol), catalysts (25 mg), solvents (5 mL), 120 ℃ and 1 h.

transfer [9,42]. Consequently, the surface-bound states of FAL and 2-PrOH on various $NiFe_2O_4$ nanocrystals were probed using ATR-IR spectra. The peak corresponding to the C═O bond in pure FAL appears at 1668 cm^{-1} (Fig. 5a). Compared with other $NiFe_2O_4$ and $NiFe_2O_4$-IQ, the C═O bond in FAL adsorbed onto $NiFe_2O_4$-Zr exhibits a noteworthy red-shift, implying a robust interaction between catalyst and C═O group. Concerning the peak related to the O-H bond in 2-PrOH (Fig. 5b), $NiFe_2O_4$-Zr also displays a most pronounced red-shift, indicating that the potent interaction between catalyst and O-H bond in 2-PrOH diminishes the energy of O-H bond. This outcome substantiates that $Zr^{>4+}$ doping promotes the catalytic ability of $NiFe_2O_4$ in 2-PrOH dissociation and substrate FAL activation. To further gain insight into the related mechanism, DFT calculations were used to demonstrate the role of $Zr^{>4+}$ doping in the adsorption process of FAL and 2-PrOH. The thermodynamically stable adsorption configurations of FAL and 2-PrOH adsorbed on Ni, Fe and Zr sites of $NiFe_2O_4$ and $NiFe_2O_4$-Zr are presented (Figure S10-S13). The acquired adsorption energies (E_{ads}) for FAL and 2-PrOH on various metal sites for $NiFe_2O_4$ and $NiFe_2O_4$-Zr demonstrate that the carbonyl oxygen in FAL and the hydroxyl oxygen in 2-PrOH exhibit stronger affinities towards Zr sites (−1.286 eV for FAL and −1.325 eV for 2-PrOH) in $NiFe_2O_4$-Zr (Figs. 4d and 4e). The adsorption results reveal a stronger interactions and bonding between substrate molecules and $NiFe_2O_4$-Zr than the other two $NiFe_2O_4$, consistent with ATR-IR analysis.

To fully understand the enhanced catalytic activity of Zr-doped $NiFe_2O_4$ for CTH of FAL, hydrogenation pathway was simulated, and the energy profiles of individual steps are presented in Figs. 4f, S14 and Table S7. In the followed calculated cases, 2 H* were directly employed for simulation instead of 2-PrOH, aiming to streamline the computational process [5]. Taking $NiFe_2O_4$-Zr as an example (Figure S14a), the reaction starts with the initial adsorption of FAL and H* onto $NiFe_2O_4$-Zr (state IS). The initial hydrogen transfer to FAL (IS→MS) occurs with a free energy (ΔG) of 1.36 eV for $NiFe_2O_4$ and 1.03 eV for $NiFe_2O_4$-Zr. The ΔG value for $NiFe_2O_4$-Zr is lower than $NiFe_2O_4$ which indicates a smaller energy barrier on $NiFe_2O_4$-Zr. Subsequently, the carbonyl oxygen underwent a further hydrogenation from MS to FS to achieve FOL with ΔG values of 0.71 eV for $NiFe_2O_4$ and 0.39 eV for $NiFe_2O_4$-Zr. In the whole hydrogenation of FAL to FOL, $NiFe_2O_4$-Zr exhibits a lower reaction ΔG compared to $NiFe_2O_4$. As anticipated, DFT results confirm that $Zr^{>4+}$ doping effectively modulates the electronic structure of $NiFe_2O_4$, enhancing interactions and bonding with substrate molecules to facilitate the reaction.

Based on the above results, the reaction process is primarily guided by Lewis acid and base sites on solid catalysts as reported elsewhere [9,11,12]. By introducing $Zr^{>4+}$ into the surface Ni_{Oh} site of $NiFe_2O_4$, surface chemical properties, especially the electronic structure, are altered. $Zr^{>4+}$ with an electron-deficient nature function as Lewis acid sites, while oxygen with an electron-rich character serves as the Lewis base site. Lewis acid site readily interacts with electron-rich oxygen in 2-PrOH and the carbonyl group of FAL, while the neighboring base site could attract the proton in the hydroxyl group, weakening the O-H bond in 2-PrOH as reported in other systems [9,10]. However, it is currently unclear whether the catalytic mechanism in CTH reaction for $NiFe_2O_4$-Zr involves a direct hydrogen transfer or indirect hydrogen transfer [43,44]. An investigation about the mechanism was carried out using an isotope-labeled 2-PrOH-d_8 GC–MS method. Replacement of 2-PrOH-d_0 with 2-PrOH-d_8 has not clarified the reaction mechanism between direct hydrogen transfer and indirect hydrogen transfer (Scheme S1). Therefore, 2-PrOH-d_8 and t-butanol at a ratio of 1:3 were employed to differentiate hydrogen transfer processes. t-BuOH lacks β-H, which makes it non-contributory as an H-donor. Even so, t-BuOH can still exchange H atoms with OD_1 groups of 2-PrOH-d_8, and active H/D of catalyst. Excess t-BuOH converts most OD_1 groups of 2-PrOH-d_8 and deuterium hydrogen bonding of metals (M-D) to OH and M-H, respectively, with the former forming 2-PrOH-d_7, which serves as the primary hydrogen donor for CTH reaction of FAL (Fig. 5d). The desired alcohols should show 1 amu MS shift (MS + 1 = 99) via direct hydrogen transfer or no shift (MS + 0 = 98) through indirect hydrogen transfer. As anticipated, GC–MS analysis clearly revealed 1 amu mass shift, confirming that FAL to FOL transformation over $NiFe_2O_4$-Zr follows the direct hydrogen transfer route.

All in all, the performance of $NiFe_2O_4$-Zr nanocrystals outperformed other reported highly efficient metal oxides, called as easy-to-separate magnetic catalysts and nanocrystal catalysts in the CTH reaction of FAL (Fig. 5c and Table S1), and our $NiFe_2O_4$-Zr catalyst possess the advantages of both types of catalysts. Notably, most of catalysts are difficult to accelerate CTH at temperature lower than 120 ℃, because of the inert surface that limits the exposure of unsaturated and acid-base active sites. In this work, we activated the surface of $NiFe_2O_4$ via quenching strategy. Doping $Zr^{>4+}$ cations onto the surface Ni_{Oh} sites changes the local electronic structure (electron-deficient $Zr^{>4+}$ and electron-rich O) and promotes the formation of highly active Lewis acid-base sites. Those Lewis acid-base sites give a robust driving force in activating small molecules, so that $NiFe_2O_4$-Zr catalyst stimulates the CTH reaction at temperature of 120 ℃, the lowest temperatures to date.

4. Conclusions

We have showcased a quenching engineering strategy that stabilizes $Zr^{>4+}$ species in $NiFe_2O_4$ nanocrystals to regulate the surface electronic structure and thereby to achieve unprecedented CTH performance. Catalyst $NiFe_2O_4$-Zr synthesized using such unique method exhibited a 94.6% conversion for hydrogenation of FAL with 2-PrOH as both solvent and H-donor within 3 h at 120 ℃, the lowest temperatures to ever reported date for the CTH reaction over metal oxides, representing a significant breakthrough in achieving an efficient catalysis by metal oxides. Leaching and recycling experiments demonstrated that the as-obtained $NiFe_2O_4$-Zr catalyst maintained an excellent catalytic performance over at least 8 cycles, exhibiting a high cyclic stability and easy separation feature. Both experimental results and theoretical calculations confirm the precise doping of $Zr^{>4+}$ to the surface octahedral Ni sites of $NiFe_2O_4$, forming $Zr^{>4+}$ with electron-deficient properties to act as strong Lewis acid sites, and oxygen with electron-rich properties to act as strong Lewis-based sites. Such unique surface chemistry enhances the interactions and bonding of $NiFe_2O_4$-Zr nanocrystals to the substrate molecules, consequently reducing the energy barrier for hydrogen transfer and ultimately expediting the reaction process. This study not only ignites novel ideas for formation of $Zr^{>4+}$ in activated metal oxides but also provides a strategic approach to explore efficient catalytic processes by controlling local electronic states.

CRediT authorship contribution statement

Xinbo Li: Writing – review & editing, Formal analysis. **Qi Wang:** Writing – review & editing, Formal analysis. **Taotao Huang:** Writing – review & editing, Formal analysis. **Mingwei Ma:** Writing – review & editing, Writing – original draft, Visualization, Validation, Methodology, Investigation, Formal analysis, Data curation, Conceptualization. **Liping Li:** Writing – review & editing, Visualization, Validation, Supervision, Resources, Funding acquisition, Conceptualization. **Zhibin Geng:** Writing – review & editing, Formal analysis. **Ge Tian:** Writing – review & editing, Resources, Formal analysis. **Guangshe Li:** Writing – review & editing, Validation, Supervision, Resources, Methodology, Funding acquisition, Formal analysis, Conceptualization.

Declaration of Competing Interest

The authors declare that they have no known competing financial interests or personal relationships that could have appeared to influence the work reported in this paper.

Data availability

Data will be made available on request.

Acknowledgements

This work was supported by the National Natural Science Foundation of China (Grant Nos. 22293041, 21871106, and U20A20246) and Jilin Provincial Science and Technology Department (SKL202302018). The authors thank beamlines MCD-A and MCD-B (Soochow Beamline for Energy Materials) at NSRL for providing beam time.

Appendix A. Supporting information

Supplementary data associated with this article can be found in the online version at 10.1016/j.apcatb.2024.123905.

References

[1] C. Xu, E. Paone, D. Rodriguez-Padron, R. Luque, F. Mauriello, Recent catalytic routes for the preparation and the upgrading of biomass derived furfural and 5-hydroxymethylfurfural, Chem. Soc. Rev. 49 (2020) 4273–4306.

[2] R. Nie, Y. Tao, Y. Nie, T. Lu, J. Wang, Y. Zhang, X. Lu, C.C. Xu, Recent advances in catalytic transfer hydrogenation with formic acid over heterogeneous transition metal catalysts, ACS Catal. 11 (2021) 1071–1095.

[3] S. Lau, D. Gasperini, R.L. Webster, Amine-boranes as transfer hydrogenation and hydrogenation reagents: a mechanistic perspective, Angew. Chem. Int. Ed. 60 (2021) 14272–14294.

[4] M.D.R. Lutz, V.C.M. Gasser, B. Morandi, Shuttle arylation by Rh(I) catalyzed reversible carbon–carbon bond activation of unstrained alcohols, Chem 7 (2021) 1108–1119.

[5] Y. Zheng, L. Wang, H. Liu, J. Yang, R. Zhang, L. Zhang, Z.A. Qiao, A modular co-assembly strategy for ordered mesoporous perovskite oxides with abundant surface active sites, Angew. Chem. Int. Ed. 61 (2022) e2022090.

[6] A.H. Valekar, M. Lee, J.W. Yoon, J. Kwak, D.-Y. Hong, K.-R. Oh, G.-Y. Cha, Y.-U. Kwon, J. Jung, J.-S. Chang, Y.K. Hwang, Catalytic transfer hydrogenation of furfural to furfuryl alcohol under mild conditions over Zr-MOFs: exploring the role of metal node coordination and modification, ACS Catal. 10 (2020) 3720–3732.

[7] J. Song, B. Zhou, H. Zhou, L. Wu, Q. Meng, Z. Liu, B. Han, Porous zirconium-phytic acid hybrid: a highly efficient catalyst for Meerwein-Ponndorf-Verley reductions, Angew. Chem. Int. Ed. 54 (2015) 9399–9403.

[8] S. Zhou, F. Dai, Z. Xiang, T. Song, D. Liu, F. Lu, H. Qi, Zirconium–lignosulfonate polyphenolic polymer for highly efficient hydrogen transfer of biomass-derived oxygenates under mild conditions, Appl. Catal. B 248 (2019) 31–43.

[9] M. Ma, P. Hou, J. Cao, H. Liu, X. Yan, X. Xu, H. Yue, G. Tian, S. Feng, Simple basic zirconium carbonate: low temperature catalysis for hydrogen transfer of biomass-derived carboxides, Green. Chem. 21 (2019) 5969–5979.

[10] M. Ma, L. Li, G. Tian, Z. Geng, X. Zhang, X. Zhao, G. Li, Creation of surface frustrated Lewis pairs on high-entropy spinel nanocrystals that boosts catalytic transfer hydrogenation reaction, Chem. Eng. J. 470 (2023) 144291.

[11] W. Fang, A. Riisager, Recent advances in heterogeneous catalytic transfer hydrogenation/hydrogenolysis for valorization of biomass-derived furanic compounds, Green. Chem. 23 (2021) 670–688.

[12] Y. Peng, C. Huang, J. Huang, M. Feng, X. Qiu, X. Yue, S. Huang, Filling octahedral interstices by building geometrical defects to construct active sites for boosting the oxygen evolution reaction on $NiFe_2O_4$, Adv. Funct. Mater. 32 (2022) 2201011.

[13] T. Zhang, Y. Liu, L. Tong, J. Yu, S. Lin, Y. Li, H.J. Fan, Oxidation state engineering in octahedral ni by anchored sulfate to boost intrinsic oxygen evolution activity, ACS Nano 17 (2023) 6770–6780.

[14] Z. Wang, P. Wu, X. Zou, S. Wang, L. Du, T. Ouyang, Z.Q. Liu, Optimizing the oxygen-catalytic performance of Zn-Mn-Co spinel by regulating the bond competition at octahedral sites, Adv. Funct. Mater. 33 (2023) 2214275.

[15] Z. Liu, Z. Kong, S. Cui, L. Liu, F. Wang, Y. Wang, S. Wang, Sq Zang, Electrocatalytic mechanism of defect in spinels for water and organics oxidation, Small (2023) 2302216.

[16] H.-Y. Wang, S.-F. Hung, H.-Y. Chen, T.-S. Chan, H.M. Chen, B. Liu, In operando identification of geometrical-site-dependent water oxidation activity of spinel Co_3O_4, J. Am. Chem. Soc. 138 (2015) 36–39.

[17] Y. Zhou, S. Sun, C. Wei, Y. Sun, P. Xi, Z. Feng, Z.J. Xu, Significance of engineering the octahedral units to promote the oxygen evolution reaction of spinel oxides, Adv. Mater. 31 (2019) 1902509.

[18] Y. Li, H. Guo, J. Zhao, Y. Zhang, L. Zhao, R. Song, Te-doped $NiFe_2O_4$ stabilized by amorphous carbon layers derived from one-step topological transitions of NiFe LDHs with significantly enhanced oxygen evolution reaction, Chem. Eng. J. 464 (2023) 142604.

[19] L. Yao, X. Wu, B. Zheng, J. Liu, Z. Geng, Y. Zhang, M. Cai, Z. Shao, M. Jiang, Y. Zhang, Y. Chen, K. Huang, S. Feng, Activating octahedral center in Co-doped $NiFe_2O_4$ via bridging amorphous MoS_x for electrocatalytic water oxidation: a case for eg orbital regulation in spinel oxide, Small Methods 7 (2023) 2201550.

[20] Y. Sun, T. Wu, Z. Bao, J. Moon, Z. Huang, Z. Chen, H. Chen, M. Li, Z. Yang, M. Chi, T.J. Toops, Z. Wu, D.E. Jiang, J. Liu, S. Dai, Defect engineering of Ceria nanocrystals for enhanced catalysis via a high-entropy oxide strategy, ACS Cent. Sci. 8 (2022) 1081–1090.

[21] Q. Ding, Y. Zhang, X. Chen, X. Fu, D. Chen, S. Chen, L. Gu, F. Wei, H. Bei, Y. Gao, M. Wen, J. Li, Z. Zhang, T. Zhu, R.O. Ritchie, Q. Yu, Tuning element distribution, structure and properties by composition in high-entropy alloys, Nature 574 (2019) 223–227.

[22] A. Bernasconi, C. Tealdi, L. Malavasi, High-temperature structural evolution in the $Ba_3Mo_{(1-x)}W_xNbO_{8.5}$ system and correlation with ionic transport properties, Inorg. Chem. 57 (2018) 6746–6752.

[23] L. Ke, S. Pang, C. Long, T. Fang, G. Yang, Y. Song, X. He, S. Ma, Y. Qian, X. Shen, C. Chen, Quenching-induced surface reconstruction of perovskite oxide for rapid and durable oxygen catalysise, Chem. Eng. J. 463 (2023) 142509.

[24] W.T. Hong, K.A. Stoerzinger, E.J. Crumlin, E. Mutoro, H. Jeen, H.N. Lee, Y. Shao-Horn, Near-ambient pressure XPS of high-temperature surface chemistry in $Sr_2Co_2O_5$ thin films, Top. Catal. 59 (2016) 574–582.

[25] N. Kozlov, O. Keßler, Influencing on liquid quenching by surface structuring, Int. J. Therm. Sci. 101 (2016) 133–142.

[26] M. Su, Z. Pan, Y. Chong, C. Ye, X. Jin, Q. Wu, Z. Hu, D. Ye, G.I.N. Waterhouse, Y. Qiu, S. Yang, Boosting the electrochemical performance of hematite nanorods via quenching-induced metal single atom functionalization, J. Mater. Chem. A 9 (2021) 3492–3499.

[27] Y. Huang, S.L. Zhang, X.F. Lu, Z.P. Wu, D. Luan, X.W. Lou, Trimetallic Spinel $NiCo_{2-x}Fe_xO_4$ nanoboxes for highly efficient electrocatalytic oxygen evolution, Angew. Chem. Int. Ed. 60 (2021) 11841–11846.

[28] M.N. Iliev, D. Mazumdar, J.X. Ma, A. Gupta, F. Rigato, J. Fontcuberta, Monitoring B-site ordering and strain relaxation in $NiFe_2O_4$ epitaxial films by polarized Raman spectroscopy, Phys. Rev. B 83 (2011) 014108.

[29] M. Satish, H.M. Shashanka, S. Saha, K. Haritha, D. Das, P.N. Anantharamaiah, C. V. Ramana, Effect of high-anisotropic Co^{2+} substitution for Ni^{2+} on the structural, magnetic, and magnetostrictive properties of $NiFe_2O_4$: implications for sensor applications, ACS Appl. Mater. Interfaces 15 (2023) 15691–15706.

[30] M.R. Anantharaman, S. Reijne, J.P. Jacobs, H.H. Brongersma, R.H.H. Smits, K. Seshan, Preferential exposure of certain crystallographic planes on the surface of spinel ferrites: a study by LEIS on polycrystalline spinel ferrite surfaces, J. Mater. Sci. 34 (1999) 4279–4283.

[31] S. Liu, K.S. Hui, K.N. Hui, V.V. Jadhav, Q.X. Xia, J.M. Yun, Y.R. Cho, R.S. Mane, K. H. Kim, Facile synthesis of microsphere copper cobalt carbonate hydroxides electrode for asymmetric supercapacitor, Electrochim. Acta 188 (2016) 898–908.

[32] Y. Cong, Q. Tang, X. Wang, M. Liu, J. Liu, Z. Geng, R. Cao, X. Zhang, W. Zhang, K. Huang, S. Feng, Silver-intermediated perovskite $La_{0.9}FeO_{3-\delta}$ toward high-performance cathode catalysts for nonaqueous lithium–oxygen batteries, ACS Catal. 9 (2019) 11743–11752.

[33] Y. Fang, L. Li, J. Yang, S. Hoang, L. Wang, J. Xu, W. Yang, C. Pan, Y. Zhu, H. Deng, Z. Luo, C. Sun, D. Gao, Z. Li, Y. Guo, Engineering the nucleophilic active oxygen species in $CuTiO_x$ for efficient low-temperature propene combustion, Environ. Sci. Technol. 54 (2020) 15476–15488.

[34] X. Li, H. Liu, Z. Chen, Q. Wu, Z. Yu, M. Yang, X. Wang, Z. Cheng, Z. Fu, Y. Lu, Enhancing oxygen evolution efficiency of multiferroic oxides by spintronic and ferroelectric polarization regulation, Nat. Commun. 10 (2019) 1409.

[35] X. Li, Y. Sun, Q. Wu, H. Liu, W. Gu, X. Wang, Z. Cheng, Z. Fu, Y. Lu, Optimized electronic configuration to improve the surface absorption and bulk conductivity for enhanced oxygen evolution reaction, J. Am. Chem. Soc. 141 (2019) 3121–3128.

[36] M. Ma, H. Liu, J. Cao, P. Hou, J. Huang, X. Xu, H. Yue, G. Tian, S. Feng, A highly efficient Cu/AlOOH catalyst obtained by in situ reduction: catalytic transfer hydrogenation of mL into γ-GVL, Mol. Catal. 467 (2019) 52–60.

[37] Y. Zheng, R. Zhang, L. Zhang, Q. Gu, Z.A. Qiao, A. Resol-Assisted, Cationic coordinative co-assembly approach to mesoporous ABO_3 perovskite oxides with rich oxygen vacancy for enhanced hydrogenation of furfural to furfuryl alcohol, Angew. Chem. Int. Ed. 60 (2021) 4774–4781.

[38] Z. He, J. Zhang, Z. Gong, H. Lei, D. Zhou, N. Zhang, W. Mai, S. Zhao, Y. Chen, Activating lattice oxygen in NiFe-based (oxy)hydroxide for water electrolysis, Nat. Commun. 13 (2022) 2191.

[39] Y. Liang, Y. Li, H. Wang, J. Zhou, J. Wang, T. Regier, H. Dai, Co_3O_4 nanocrystals on graphene as a synergistic catalyst for oxygen reduction reaction, Nat. Mater. 10 (2011) 780–786.

[40] W. Song, A.S. Poyraz, Y. Meng, Z. Ren, S.-Y. Chen, S.L. Suib, Mesoporous Co_3O_4 with controlled porosity: inverse micelle synthesis and high-performance catalytic CO oxidation at -60 °C, Chem. Mater. 26 (2014) 4629–4639.

[41] Y. Wang, H. Liu, J. Zhang, Y. Cheng, W. Lin, R. Huang, L. Peng, Direct epitaxial synthesis of magnetic biomass derived acid/base bifunctional zirconium-based hybrid for catalytic transfer hydrogenation of ethyl levulinate into γ-valerolactone, Renew, Energy 197 (2022) 911–921.

[42] Y. Ren, Y. Yang, L. Chen, L. Wang, Y. Shi, P. Yin, W. Wang, M. Shao, X. Zhang, M. Wei, Synergetic effect of Cu^0-Cu^+ derived from layered double hydroxides toward catalytic transfer hydrogenation reaction, Appl. Catal. B 314 (2022) 121515.

[43] M.J. Gilkey, P. Panagiotopoulou, A.V. Mironenko, G.R. Jenness, D.G. Vlachos, B. Xu, Mechanistic insights into metal lewis acid-mediated catalytic transfer hydrogenation of furfural to 2-methylfuran, ACS Catal. 5 (2015) 3988–3994.

[44] M. Ma, X. Yan, P. Hou, J. Cao, H. Liu, X. Xu, H. Yue, Ge Tian, S. Jing, S. Feng, One-pot transfer hydrogenation of methyl levulinate into valerolactone and 1,4-pentanediol over insitu reduced $Cu/ZrOCO_3$ in 2-PrOH, ChemistrySelect 5 (2020) 924–930.